Computer-Aided Civil and Infrastructure Engineering 42 (2026) 100023

Contents lists available at ScienceDirect

Computer-Aided Civil and Infrastructure Engineering

journal homepage: www.sciencedirect.com/journal/computer-aided-civil-and-infrastructure-engineering

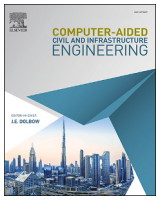

Research Article

A fast and accurate phase-based displacement measurement method based on complex Laplacian pyramid with condensed focus frequency

Sida Ai [a], Chuanzhi Dong [b], Qipei Mei [a,*]

[a] Department of Civil and Environmental Engineering, University of Alberta, Edmonton, Canada
[b] Department of Computer Science, The University of Texas at Austin, Austin, TX 78712, USA

A B S T R A C T

The phase-based displacement measurement method has received increasing attention due to its high subpixel accuracy and robustness against illumination variations. However, its overall performance is constrained by the computational inefficiency introduced by the additional phase extraction step. Recent studies have attempted to improve computational efficiency by proposing new phase extraction techniques, but these approaches often suffer from limited robustness, leading to reduced measurement accuracy. To overcome this limitation, a novel phase extraction method is developed to preserve the high measurement accuracy of traditional phase-based methods while significantly enhancing computational efficiency. Featuring a simple mathematical structure and a condensed focus frequency at each scale level of the Laplacian pyramid, the proposed Complex Laplacian Pyramid with Condensed Focus Frequency (CLP-CFF) method achieves a better balance between accuracy and efficiency than existing phase-based methods. The accuracy, computational efficiency, and robustness of the CLP-CFF method are further validated through laboratory and real-world experiments.

1. Introduction

In the field of structural health monitoring, the displacement of structures is an important parameter. It can be used for studying the dynamic properties of structures, assessing load levels, and evaluating their health conditions (Javadinasab Hormozabad et al., 2021; Perez-Ramirez et al., 2019). Civil structures carry various loads during their lifetime, such as traffic, earthquake, and wind loads. The monitoring of structural responses under these loads, whether in field or laboratory experiments, is critical to assess the health condition of structures and ensure safe operation (Amezquita-Sanchez & Adeli, 2019; Oh et al., 2017).

Conventional displacement measurement techniques are generally categorized into two groups: contact-based and non-contact-based approaches. Contact-based methods, such as linear variable differential transformers (LVDTs) and draw-wire displacement sensors, are commonly used (Gomez et al., 2018; Saxena & Seksena, 1989). However, these techniques often introduce additional mass or force to the structure, which may affect the accuracy of dynamic behavior analysis and load evaluation. In comparison, non-contact methods eliminate these drawbacks. One example is the GPS-based displacement measurement approach, which, despite being non-invasive, suffers from limited precision, typically restricted to the centimeter level (Feng & Feng, 2016). Another non-contact option is the Laser Doppler Vibrometer (LDV), which offers high measurement accuracy, although it comes at a substantial cost (Chen et al., 2018).

In recent years, advancements in computer vision and computational power have led to growing interest in vision-based approaches for displacement measurement (Pan et al., 2023; Park et al., 2015). As a type of non-contact technique, vision-based methods provide several advantages, including low installation labor, extended measurement range, and enhanced accuracy and robustness, especially when integrated with well-designed computer vision algorithms (Feng & Feng, 2018; Xu & Brownjohn, 2018).

The algorithm of displacement measurement is the most important step in the vision-based method, which affects the accuracy, robustness, and efficiency of the vision-based method (Feng & Feng, 2018; Luo & Feng, 2018). Therefore, the investigation and development of algorithms for vision-based methods are the main focus of our study. In general, the algorithms for vision-based displacement measurement can be divided into two groups, the intensity-based methods and the phase-based methods (Miao et al., 2023).

The intensity-based methods include template matching, feature point matching, digital image correlation (DIC), intensity-based optical flow, and, deep learning-based method (Dong & Catbas, 2021). The traditional optical flow method can estimate the displacement field of a video at subpixel level, but it relies on the assumptions of constant intensity and small motion (Horn & Schunck, 1981). Under these

* Corresponding author.
E-mail address: qipei.mei@ualberta.ca (Q. Mei).

https://doi.org/10.1016/j.cacaie.2026.100023
Received 21 December 2025; Accepted 12 February 2026
Available online 19 March 2026

conditions, the method cannot uniquely determine motion because it has two unknown velocity components but only one constraint. To overcome this limitation, the Lucas-Kanade (LK) optical flow method assumes that all pixels within a small region move in the same way, which enables a more stable solution (Lucas & Kanade, 1981). Although this improves robustness, its performance still decreases when the motion becomes large. Deep learning-based methods have recently achieved significant progress in optical flow estimation. One representative approach is the Recurrent All Pairs Field Transforms (RAFT) method, which calculates the similarity between all pixel pairs in two frames and then refines the motion prediction through iterative updates (Teed & Deng, 2020). This strategy allows the method to capture both large movements and fine details more effectively than earlier techniques. Overall, the intensity-based displacement measurement algorithms are highly sensitive to changes in illumination, necessitating the careful preparation of lighting and high-contrast markers, which requires extensive preparatory work.

In addition to intensity, phase represents a critical attribute of images, conveying the position of waveform elements within their oscillation cycles (Morrone et al., 1986). Due to its relative invariance to illumination changes and strong capability in revealing structural characteristics, phase information proves especially valuable for tasks like feature detection, motion magnification and displacement measurement (Cai et al., 2023; Fleet & Jepson, 1990; Morrone & Owens, 1987). Recently, phase-based displacement measurement has attracted increasing attention for its robustness to illumination variations and its capability to achieve high-precision subpixel accuracy (Barron et al., 1994; Collier & Dare, 2022; Diamond et al., 2017; Fleet & Jepson, 1990).

Although phase-based methods offer significant advantages, they are often hindered by high computational demands (Luan et al., 2021; Simoncelli & Freeman, 1995; Yang & Tse, 2021). Nonetheless, computational efficiency remains a key requirement in vision-based displacement measurement, especially in scenarios such as real-time monitoring, high-resolution video analysis, and long-duration tracking, where high computational efficiency is essential (Feng & Feng, 2018; Ma, Choi, & Sohn, 2022).

Typically, phase-based displacement measurement consists of two primary stages: phase extraction and the calculation of phase-based optical flow (Fleet & Jepson, 1990). Among these, the phase extraction step is the most computationally demanding, as it involves applying a filter to each video frame through convolution operations (Fleet & Jepson, 1990; Simoncelli et al., 1992). However, the choice of phase extraction technique is flexible, since a variety of algorithms have been employed for displacement measurement (Chen et al., 2014; Fleet & Jepson, 1990).

Current phase extraction methods can generally be divided into two main categories: traditional methods, such as the Gabor wavelet and complex steerable pyramid (CSP), and recently developed methods (Chen et al., 2015; Fleet & Jepson, 1990; Li et al., 2023; Liu et al., 2022; Liu et al., 2024). Traditional phase extraction methods have been extensively validated in various applications and estimation tasks, demonstrating high robustness and accuracy (Collier & Dare, 2022; Diamond et al., 2017; Ma, Choi, Liu, et al., 2022; Miao et al., 2022; Shang & Shen, 2018). However, they suffer from computational inefficiency due to their complex mathematical formulations and the overcomplete representation of the original signal (Movellan, 2002; Simoncelli & Freeman, 1995). To address this limitation, recently developed methods have been proposed to address this limitation, particularly by simplifying parameter selection and phase extraction processes. These methods include the Hilbert and Riesz transform-enhanced methods, and derivative-enhanced methods (Li et al., 2023; Liu et al., 2022; Liu et al., 2024). Nevertheless, they have not been widely validated through diverse applications, and their robustness and accuracy may be inferior to those of traditional methods, due to unfavorable designs or inherent properties in their strategies or mathematical frameworks. Some of them may also fail to significantly improve computational efficiency. In particular, for the Hilbert and Riesz transform-enhanced methods, the use of bandpass filtering and direct application to full-resolution signals results in only limited improvements compared to traditional methods.

In light of the above discussion, methodological innovation in phase-based displacement measurement does not necessarily require the development of an entirely new mathematical transform. Instead, many widely adopted phase extraction techniques, such as the Gabor wavelet and the CSP, were originally developed for general signal or image analysis and later adapted for displacement measurement tasks. Accordingly, the integration and optimization of existing mathematical tools for phase extraction represent a practical and effective direction for advancing phase-based displacement measurement methods.

Therefore, it would be helpful to further improve the overall performance of phase extraction methods by proposing a new approach that achieves a better balance between accuracy and computational efficiency compared to all existing methods, including both traditional and recently developed ones, while maintaining sufficient robustness. Improving the overall performance of phase-based methods would provide a solid foundation for achieving accurate and real-time phase-based displacement monitoring. Under such circumstances, the Complex Laplacian Pyramid with Condensed Focus Frequency (CLP-CFF) method is proposed in this work as a new phase extraction method with improved overall performance. The CLP-CFF method features a simple mathematical framework and accurate phase extraction, which significantly improves computational efficiency and maintains accuracy comparable to that of traditional phase extraction methods.

The structure of this paper is organized as follows: Section 2 introduces the phase extraction and displacement measurement processes of the CLP-CFF phase-based optical flow. Section 3 presents the experimental validation of the CLP-CFF method, including laboratory and outdoor experiments. Further comparisons of measurement performance with other vision-based methods are also provided to demonstrate its superior overall performance.

2. Methodology

The CLP-CFF method is developed based on the Laplacian pyramid, which functions as a bandpass filter to facilitate phase extraction. To improve displacement measurement accuracy, the focus frequency at each pyramid scale is optimized, resulting in the Laplacian pyramid with Condensed Focus Frequency (LP-CFF). By further applying the Hilbert transform to each LP-CFF subband, the CLP-CFF method is obtained. Its accuracy and efficiency are experimentally validated in both laboratory and outdoor settings through comparison with other vision-based approaches.

Fig. 1 summarizes the operational framework of the CLP-CFF method for phase-based displacement measurement. The procedure begins with the video input, followed by constructing an LP-CFF on each frame, which functions as a bandpass filter to aid phase extraction. The high-pass residual subband (L) is then obtained from the pyramid. A Hilbert transform is applied to this subband to generate the Hilbert pairs along the vertical and horizontal directions, denoted as LV_h and LH_h, respectively. These components are subsequently combined to construct the CLP-CFF, where $LV_c = L + LV_h$ and $LH_c = L + LH_h$, providing the analytic signals for phase extraction. The vertical and horizontal phase components (ϕ_V and ϕ_H) are then extracted from the analytic signals for displacement measurement. Finally, an estimation of the optical flow from the phase fields ϕ_V and ϕ_H enables the subsequent retrieval of the displacement signal.

2.1. The Laplacian pyramid with condensed focus frequency for accurate phase extraction

Originating from Burt and Adelson's study (Burt & Adelson, 1987), the Laplacian pyramid constitutes a compact image coding method

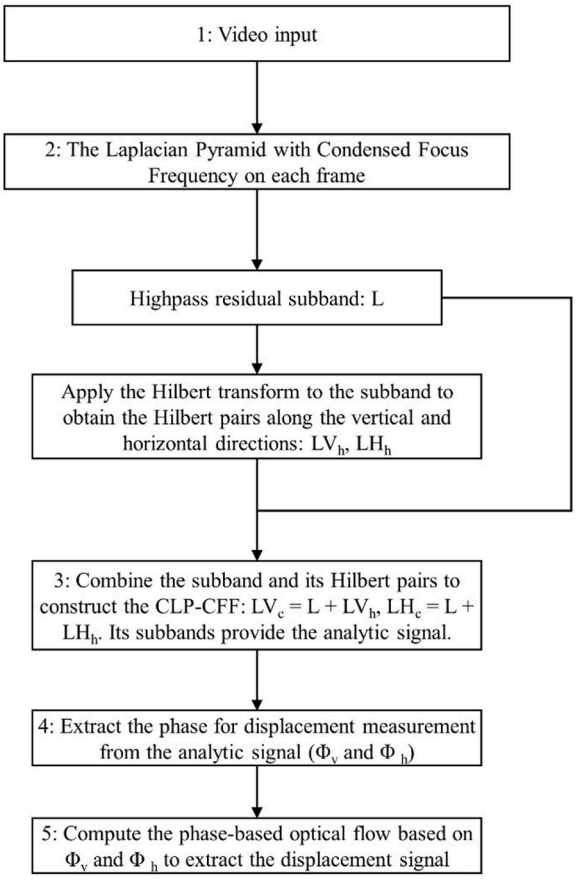

Fig. 1. The flowchart of the CLP-CFF method.

designed to enhance the efficiency of image compression. It represents images in a multiscale, band-pass form that is both redundant and sparse, enabling progressive transmission and efficient storage. Unlike the Gaussian Pyramid, which only smooths and downsamples an image, the Laplacian pyramid explicitly stores band-pass residuals at each scale, enabling perfect reconstruction when combined with the corresponding Gaussian base layer.

The key design principle of the Laplacian pyramid lies in its ability to decompose an image into multiple frequency bands while retaining a compact representation. This is achieved by recursively applying Gaussian low-pass filters and downsampling, followed by differencing with the upsampled version of the next layer, yielding the Laplacian (i.e., high-frequency residual) pyramid:

As shown in Fig. 2, the construction of the Laplacian pyramid begins with generating a Gaussian pyramid by successively applying Gaussian smoothing followed by downsampling. Each layer Gi in the Gaussian pyramid corresponds to an image of reduced resolution derived from the initial image G0. To compute the Laplacian pyramid, each Gaussian level Gi is expanded (i.e., upsampled and smoothed) to match the size of the previous level Gi-1. The expanded image is then subtracted from Gi-1, producing a band-pass image Li-1 that captures the image details lost between scales. This difference image represents the Laplacian level. The process continues recursively, and the coarsest Gaussian level (e.g., G3 in the figure) is preserved as the top level L3 of the Laplacian pyramid to retain low-frequency information. This hierarchical representation enables efficient multiscale analysis and reconstruction, as the original image can be perfectly reconstructed by reversing the process, adding each Laplacian level to the expanded version of the next level.

The original construction of the Laplacian pyramid uses a fixed Gaussian kernel, typically with a standard deviation $\sigma = 1$, to ensure reconstruction fidelity across scales (Burt & Adelson, 1987). This choice of $\sigma = 1$ corresponds to a frequency octave bandwidth of approximately one-half Nyquist, which aligns with the multiscale decomposition concept and allows the residuals at each level to span distinct, non-overlapping frequency bands.

As a compact and efficient image coding technique, the Laplacian pyramid has received limited attention in the field of displacement measurement, particularly in phase-based displacement measurement. However, it is fundamentally a multiscale image representation designed to capture both spatial and frequency domain features in a redundant yet sparse form. This suggests its potential utility as a band-pass filtering structure for phase extraction in displacement measurement applications. Therefore, we explore the potential of applying the Laplacian pyramid for phase extraction in the context of displacement measurement.

As shown in Fig. 3, the Gaussian filter does not exhibit a hard cutoff in its frequency response; instead, its magnitude gradually diminishes as the frequency increases. In practical implementations, setting $\sigma = 1$ ensures that the residual band spans a frequency octave from approximately 0.25 to 0.5. This decomposition behavior enables a smooth and continuous partitioning of the frequency content across pyramid levels, as summarized in Table 1.

As observed in Table 1, the highpass residual bands of the Laplacian pyramid are designed to cover the upper half of the expressible frequency range at each level. While this is ideal for image reconstruction, it can introduce drawbacks for phase-based displacement measurement.

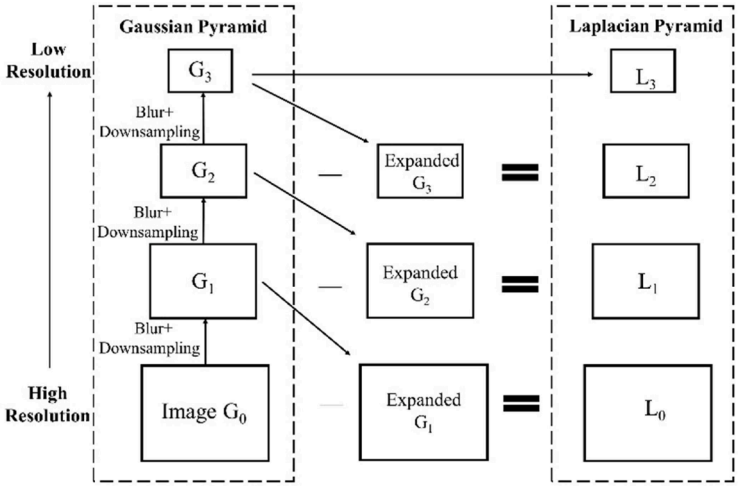

Fig. 2. The framework of Laplacian pyramid.

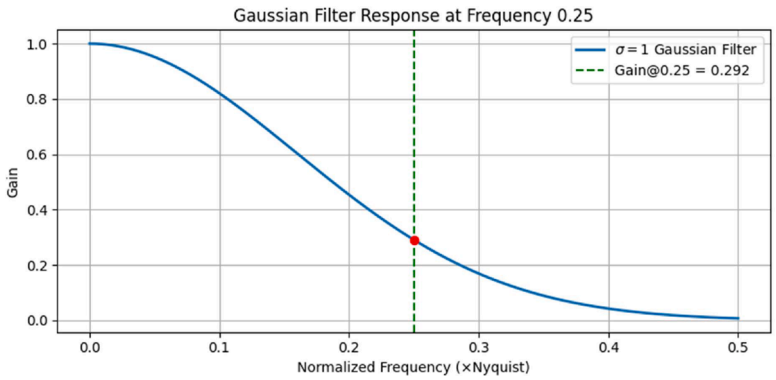

Fig. 3. The frequency spectrum of a Gaussian filter with a standard deviation of 1.

Table 1
The expressible frequency range and highpass residual band's focus frequency range under different scale levels of a standard Laplacian pyramid.

Level	Scale	Nyquist (Relative to Original)	Expressible Frequency Range	Highpass Residual Band (Relative to Original)
L0	1 ×	0.5	[0, 0.5]	[0.25, 0.5]
L1	1/2 ×	0.25	[0, 0.25]	[0.125, 0.25]
L2	1/4 ×	0.125	[0, 0.125]	[0.0625, 0.125]
L3	1/8 ×	0.0625	[0, 0.0625]	[0.03125, 0.0625]

On the one hand, high-frequency components are more susceptible to noise, which can interfere with the target localization (Miao et al., 2023). On the other hand, the wide frequency bandwidth of the high-pass residual is not well-suited for Hilbert transform analysis, which theoretically performs most reliably on signals that are approximately monofrequency (Cohen, 1995; Liu et al., 2022).

To make the high-pass residual bands more compatible with phase-based displacement measurement, the focus frequency range must be adjusted. For generating stable and accurate phase information for displacement measurement, the mid-frequency range of the expressible spectrum is most suitable. This is because high frequency components tend to introduce noise. Low frequency components cause severe edge blurring, which adversely affects target localization, and lead to a slowly varying phase that is insensitive to small motions. Moreover, when the focus frequency range is adjusted to the middle part of the expressible frequency range, the bandwidth of the high-pass residual is reduced compared to that of the standard Laplacian pyramid, which in turn facilitates a more accurate Hilbert transform.

Therefore, we propose a Laplacian pyramid with a condensed focus frequency band to generate more accurate phase information for displacement measurement. To achieve this condensed frequency focus, the standard deviation of the Gaussian filter can be adjusted accordingly.

In this study, the practical cutoff frequency is defined using a fixed gain threshold. A reference gain value Gth≈0.292 is obtained from the Gaussian response with $\sigma = 1$ at a normalized frequency of 0.25. For an arbitrary σ, the practical cutoff frequency is defined as the smallest frequency at which the filter gain falls below Gth. In the discrete implementation, the cutoff is determined by searching the discrete frequency grid for the first bin satisfying this criterion; linear interpolation between adjacent bins may be used to improve accuracy if needed.

As presented in Fig. 4, by increasing the standard deviation to around 2.08, the practical cutoff frequency is reduced to approximately 0.12. This adjustment effectively centers the high-pass residual's frequency response around the middle of its expressible frequency range while maintaining a relatively narrow bandwidth for all levels beyond level 0, as shown in Table 2.

Table 2
The expressible frequency range and highpass residual band's focus frequency range under different scale levels of a Laplacian pyramid with condensed focus frequency.

Level	Scale	Nyquist (Relative to Original)	Expressible Frequency Range	Highpass Residual Band (Relative to Original)
L0	1 ×	0.5	[0, 0.5]	[0.12, 0.5]
L1	1/2 ×	0.25	[0, 0.25]	[0.06, 0.12]
L2	1/4 ×	0.125	[0, 0.125]	[0.03, 0.06]
L3	1/8 ×	0.0625	[0, 0.0625]	[0.015, 0.03]

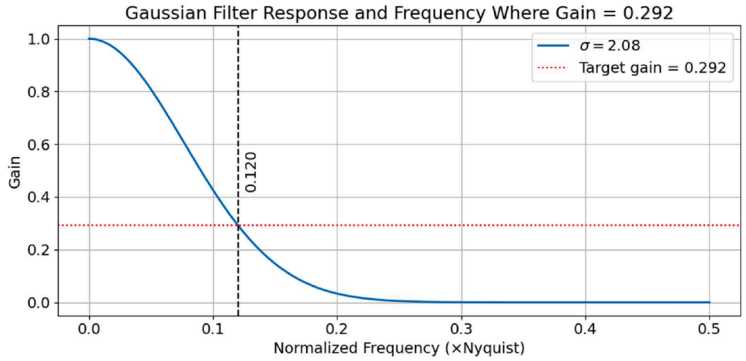

Fig. 4. The frequency spectrum of a Gaussian filter with a standard deviation of 2.08.

It is worth noting that lowering the focus frequency band (higher standard deviation of the Gaussian filter) also results in a narrower passband, which introduces a trade-off between the accuracy of the Hilbert transform and the sensitivity to micro-motion. Based on our practical application experience as stated in Section 3, it is recommended to select a standard deviation between 2.0 and 2.8 to balance noise suppression, phase fidelity, and motion sensitivity, considering the specific video conditions.

2.2. The construction of the CLP-CFF

After applying the LP-CFF to decompose each video frame into multiple scale levels, the Hilbert transform is employed to construct the CLP-CFF.

As shown in Eq. (1), the Hilbert transform is applied along the columns of each subband L to obtain its Hilbert pair LV_h, representing the vertical direction. The original subband L is then treated as the real part, while the vertical Hilbert pair LV_h serves as the imaginary part, forming a complex subband LV_c, as defined in Eq. (2), which constitutes one component of the CLP-CFF.

$$LV_h(x_i,y,t) = \frac{1}{\pi}\int \frac{L(x_i,\tau,t)}{y-\tau}d\tau \tag{1}$$

$$LV_c(x_i,y,t) = L(x_i,y,t) + jLV_h(x_i,y,t) \tag{2}$$

Based on the same subband L, the Hilbert transform is applied to each row of L to obtain the horizontal Hilbert pair LH_h, as illustrated in Eq. (3). The subband L and its horizontal Hilbert pair are then combined to construct the complex subband LH_c for the CLP-CFF, as shown in Eq. (4). This complex subband also provides the analytic signal.

$$LH_h(x,y_i,t) = \frac{1}{\pi}\int \frac{L(\tau,y_i,t)}{x-\tau}d\tau \tag{3}$$

$$LH_c(x,y_i,t) = L(x,y_i,t) + jLH_h(x,y_i,t) \tag{4}$$

The subbands LV_c and LH_c constitute the CLP-CFF. The method is named CLP-CFF because the transformation process from LP-CFF to CLP-CFF is analogous to the conversion of the steerable pyramid into the CSP, which also employs the Hilbert pairs of each subband as the imaginary part of the CSP. Overall, the CLP-CFF produces complex subbands that serve as analytic signals, from which the instantaneous phase can be extracted for displacement measurement.

From an algorithmic perspective, the proposed CLP-CFF method is symmetric with respect to the horizontal and vertical directions due to identical Hilbert-based constructions applied along image rows and columns. As a result, no inherent orientation bias is introduced for frames with isotropic spatial sampling. In practice, however, minor orientation-related effects may arise under anisotropic spatial sampling due to differences in discrete frequency resolution and boundary effects associated with the Hilbert transform.

2.3. The phase extraction and displacement computation processes

The instantaneous phase ϕ_V in the vertical direction is obtained by evaluating the phase angle (argument) of the complex subband LV_c in CLP-CFF, as shown in Eq. (5). Following the same way, the horizontal phase ϕ_H is also obtained, as illustrated in Eq. (6).

$$\phi_V(x_i,y,t) = \arg(LV_c(x_i,y,t)) = \arctan\left(\frac{LV_H(x_i,y,t)}{L(x_i,y,t)}\right) \tag{5}$$

$$\phi_H(x,y_i,t) = \arg(LH_c(x,y_i,t)) = \arctan\left(\frac{LH_H(x,y_i,t)}{L(x,y_i,t)}\right) \tag{6}$$

After extracting the phase from the CLP-CFF, phase-based optical flow can be employed to compute the displacement. The procedure for deriving optical flow from phase information has been presented in Ai et al. (2025). For completeness, we only present the final equations in Eqs. (7)–(9).

$$\vec{v}_c = -\frac{\phi_t}{(\phi_x{}^2+\phi_y{}^2)}(\phi_x,\phi_y) \tag{7}$$

$$\vec{v}_{cH} = -\frac{\phi_t}{(\phi_x{}^2)}(\phi_x,0) = -\frac{\phi_t}{(\phi_x{}^2)}\left(\frac{d\phi_H}{dx},0\right) \tag{8}$$

$$\vec{v}_{cV} = -\frac{\phi_t}{(\phi_y{}^2)}(0,\phi_y) = -\frac{\phi_t}{(\phi_y{}^2)}\left(0,\frac{d\phi_V}{dy}\right) \tag{9}$$

The spatial phase gradients in the horizontal and vertical directions are expressed as ϕ_x and ϕ_y, respectively, whereas ϕ_t characterizes the temporal variation of phase. $\vec{v}_c$ is the component velocity of phase-based optical flow between two frames. The decomposition of the velocity into horizontal and vertical directions is expressed as $\vec{v}_{cH}$ and $\vec{v}_{cV}$.

The motion of each pixel can be inferred by combining its velocity with the temporal gap between frames, yielding the displacement described in Eq. (10). It should be noted that, for structural displacement measurement, the sampling rate and motion frequency determine the adequacy of motion capture and the validity of the recorded motion video, rather than directly influencing the proposed displacement extraction algorithm.

$$\vec{d}_{cH} = \vec{v}_{cH}\Delta t,\ \vec{d}_{cV} = \vec{v}_{cV}\Delta t \tag{10}$$

3. Experimental verification

3.1. Verification experiment on a column fixed on a shaker

To evaluate the effectiveness of the proposed CLP-CFF method, a vision-based displacement measurement experiment was conducted. In this experiment, a column is affixed to the end of a shaker, which generates unidirectional reciprocating motion. Ground truth displacement data are obtained using a laser displacement sensor from the Keyence LK-G3000 series, and an iPhone 11 camera records the motion video at 24 FPS with 720p resolution. The layout and schematic diagram of this experiment are shown in Fig. 5(a) and (b), respectively.

The experimental setup ensures that the camera's optical axis is oriented orthogonally to the direction of motion of the vibrating column. The camera is placed at a fixed distance of 900 mm from the target. With a focal length configured at 52 mm, the imaging system achieves a spatial resolution of approximately 0.402 mm per pixel. At the start of the recording, the column is positioned centrally within the field of view, as illustrated in the initial image frame of the video sequence in Fig. 6.

As mentioned in Section 2.1, the Condensed Focus Frequency brings many advantages for phase-based displacement measurement. However, the standard deviation range that can really improve measurement accuracy still needs to be determined based on the results of real-life applications. Therefore, we selected a range of standard deviation values for computation, starting from the standard Laplacian pyramid with a standard deviation of 1 and gradually increasing up to a standard deviation of 3.5. By doing so, we can, on one hand, reveal how the actual measurement accuracy varies with the standard deviation, thereby verifying our previous theoretical assumptions. On the other hand, this approach allows us to identify an optimal standard deviation and a practical application range, which can provide valuable guidance for real-world implementations.

As observed from Table 3, starting from the standard Laplacian pyramid (standard deviation = 1), the MAE value decreases as the standard deviation increases, reaching its minimum at 2.35. Beyond this point, the MAE value begins to increase with further growth in the standard deviation.

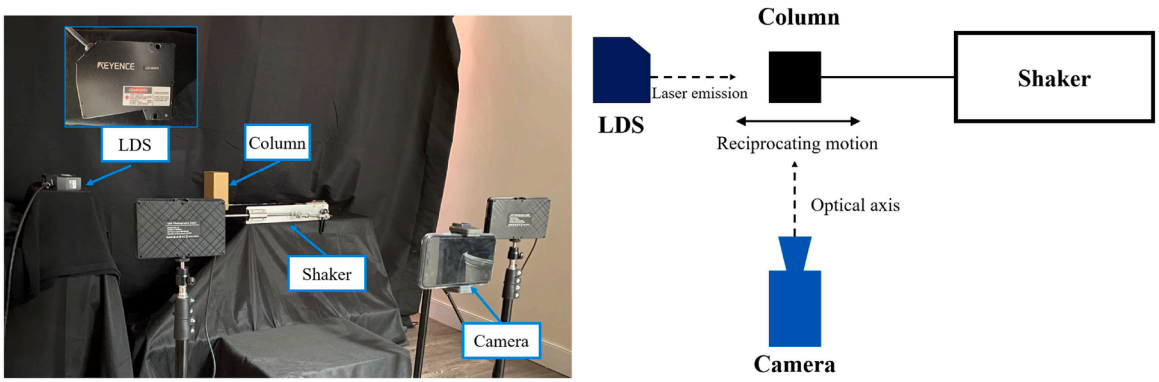

(a) Experiment layout (b) Schematic diagram

Fig. 5. Images of the experiment layout and schematic diagram.

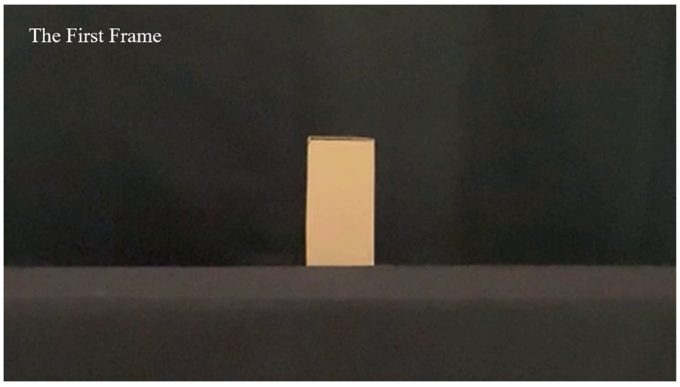

Fig. 6. The first frame of the recorded motion video.

Table 3
The measurement performance of the CLP-CFF method with various standard deviations.

Standard Deviation	1.00	1.20	1.50	1.80	2.00	2.10	2.20	2.30	2.35
MAE (mm)	0.6225	0.5036	0.3570	0.3261	0.2819	0.2659	0.2524	0.2453	0.2446
Standard Deviation	2.40	2.50	2.60	2.70	2.80	2.90	3.00	3.20	3.50
MAE (mm)	0.2456	0.2537	0.2698	0.2906	0.3149	0.3422	0.3720	0.4363	0.5393

The results also confirmed that the Condensed Focus Frequency indeed improves measurement accuracy compared to the standard Laplacian pyramid. Within the tested range, the calculated accuracy exhibits an extremum and maintains generally good performance. In particular, a certain subrange (2.0–2.8) demonstrates a stable superiority over other methods in

Table 4, with the optimal values generally falling within this interval. Therefore, this range can be regarded as the practical application range, as it typically provides relatively accurate and reliable measurement results. The MAE from the extremum point (standard deviation = 2.35) is selected for the comparison in the following parts.

The measurement time history results of the CLP-CFF method are presented in Fig. 7. As observed, they closely match the displacement ground truth. Phase-based optical flow methods based on existing phase extraction techniques, together with widely used intensity-based methods, are employed for comparison. The compared methods include Gabor wavelet transform, CSP, Hilbert transform–enhanced, Riesz transform–enhanced, derivative-enhanced methods, LK optical flow, template matching, and RAFT optical flow.

For the Gabor wavelet transform, CSP, Hilbert transform-enhanced, Riesz transform-enhanced, derivative-enhanced, and CLP-CFF methods, the points of interest (POIs) are set at the center of the target. Meanwhile, in the LK and RAFT optical flow methods, the feature point is set at the edge of the target, where the feature is strong regarding the motion direction. For template matching, the whole target is selected as the template.

With respect to parameter configuration, regarding the Gabor wavelet and CSP methods, the center frequency and scale level were mainly adjusted to match the motion region. The optimal center frequency and scale level were obtained by comparison with the ground truth. Regarding the Hilbert- and Riesz-transform-enhanced methods, the peak frequency selection strategy proposed in the original work was

Table 4
The vision-based methods measurement performances for the experiment case.

	CSP	Gabor	Hilbert	Riesz	Derivative	LK	TM	RAFT	CLP-CFF
MAE (mm)	0.2571	0.2269	0.3635	0.7234	9.9684	0.4627	0.5119	0.3736	0.2446

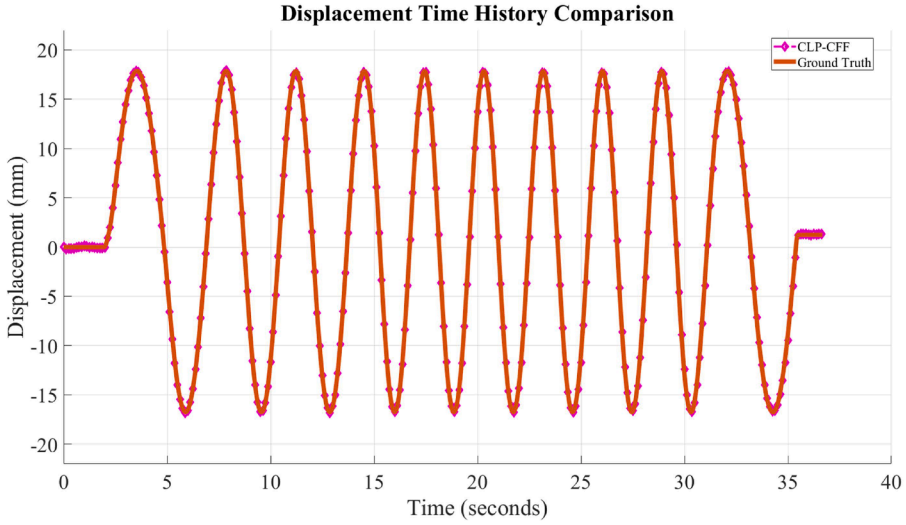

Fig. 7. Comparison of displacement history between CLP-CFF and laser measurements.

employed.

The comparisons of displacement time histories are presented in Fig. 8. The MAE results and comparison are presented in Table 4. The CLP-CFF method exhibits comparable measurement accuracy to CSP and Gabor wavelet methods and clearly outperforms the recently developed phase-based methods in this scenario.

The higher accuracy of the CLP-CFF method compared to the Hilbert transform-enhanced and Riesz transform-enhanced methods can be attributed to its mathematical framework, which is similar to CSP. In this framework, the scale level is used to fit the motion region, whereas other methods rely on peak frequency selection as the key parameter-setting strategy, which may be affected by noise and pick a less accurate target frequency. In contrast, the derivative-enhanced method fails in this measurement task, exhibiting an extremely high MAE value, which may be caused by its low robustness. In comparison with intensity-based methods, the CLP-CFF method, as a phase-based method, still demonstrates higher measurement accuracy.

For a fair comparison of computational speed, all methods were evaluated under consistent hardware conditions. Specifically, all vision-based methods except RAFT were computed using a single core of an AMD Ryzen 9 5900 processor (3.0 GHz base clock and 4.7 GHz max boost) in a system equipped with 32 GB of DDR4 RAM (3200 MHz). The RAFT optical flow method, due to its GPU-oriented design, was performed on an NVIDIA GeForce RTX 3080 GPU (10 GB memory) with CUDA acceleration. The total number of frames in the processed video in this section is 891. The processing time and speed are presented in Table 5. As shown in Table 5, CLP-CFF achieves a significant computational advantage. While not as fast as the intensity-based methods, it completes processing in approximately 40 seconds, making it the fastest among all phase-based methods. Regarding the RAFT optical flow method, although GPU acceleration is employed, the computational speed is still relatively slow. This is because RAFT computes full-field displacement, whereas the other methods estimate displacement only at the POI or within a subregion of the frame.

The superior performance of CLP-CFF for this experiment can be explained as follows:

Accuracy: The use of a Gaussian filter with $\sigma = 2.35$ ensures that the residual band lies within the middle frequency range of each level. This avoids noisy high-frequency components and slow-varying low-frequency content, providing smoother and more accurate phase signals. Narrower bandwidth also favors the Hilbert transform, which theoretically performs best on near-monofrequency signals.

Speed: Unlike Gabor and CSP, CLP-CFF avoids complex kernel convolutions or steerable filtering. It uses FFT-based Gaussian filtering with a much simpler structure, reducing the computational load. Compared with other Hilbert- or Riesz-enhanced methods, the Gaussian filter has a

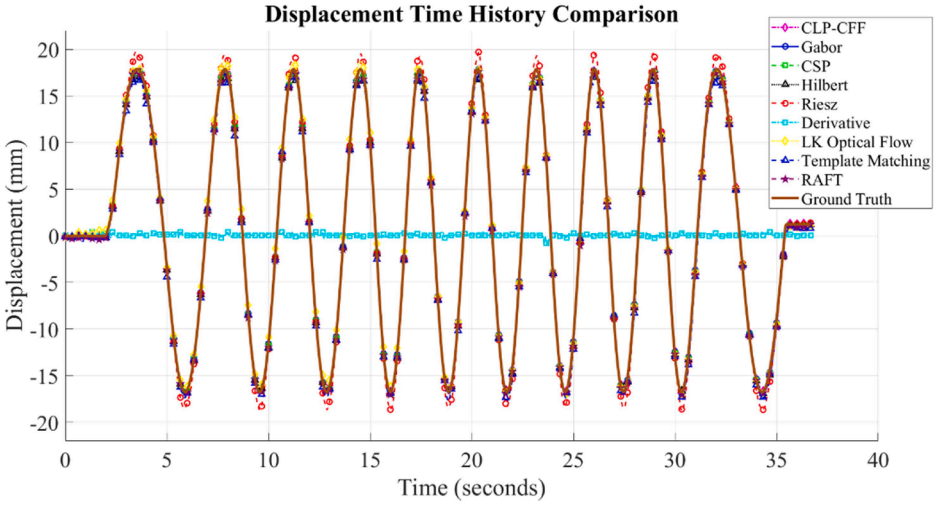

Fig. 8. Comparison of displacement history between vision-based methods and laser measurements.

Table 5
The computation time comparison of different vision-based methods for the laboratory experiment.

	CSP	Gabor	Hilbert	Riesz	Derivative	LK	TM	RAFT	CLP-CFF
Computation time (seconds)	220.3757	264.4236	185.5473	176.7931	61.5910	15.2792	14.9846	198.2782	39.3967
Processing speed (ms/frame)	247.3352	296.7717	208.2461	198.4210	69.1257	17.1484	16.8177	222.5345	44.2163

simpler mathematical formulation than the Butterworth filter, while the pyramid-based approach reduces the computational cost of phase estimation on the full-resolution signal. These findings validate CLP-CFF as an accurate and efficient alternative for phase-based displacement measurement.

A weighted and dimensionless Performance Efficiency Index (PEI) is proposed in Eq. (11) to evaluate the performance of various algorithms by taking both measurement accuracy and computational efficiency into account. In this metric, the MAE and computation time are normalized using reference values of 1 mm and 1 second, respectively. The influence of accuracy and efficiency is modulated through weighting coefficients α and β, respectively, allowing flexible prioritization depending on specific application needs. A higher PEI score corresponds to a more favorable balance between accuracy and computational efficiency.

$$PEI_{\alpha,\beta} = \frac{1}{\mathrm{MAE}_{\mathrm{norm}}^{\alpha} \cdot \mathrm{Time}_{\mathrm{norm}}^{\beta}} \tag{11}$$

For phase-based methods, an additional phase extraction step is inherently required compared with conventional intensity-based methods, which inevitably leads to lower computational efficiency. However, phase-based methods are primarily valued for their robustness and high accuracy. Therefore, maintaining accuracy is prioritized, and improvements in computational speed are pursued only insofar as accuracy is preserved. Consequently, when determining the PEI parameter, greater emphasis is placed on accuracy. Accordingly, $\alpha = \{1,2,4,6\}$ and $\beta = 1$ are chosen to assign greater weight to accuracy in the overall performance evaluation.

As observed from Table 6, CLP-CFF achieves the highest PEI values among all existing phase-based methods across all cases. This indicates that the CLP-CFF method provides the best overall performance in terms of efficiency and accuracy among phase-based methods.

However, when $\alpha = 1$ and $\beta = 1$, some intensity-based methods, including the LK optical flow and template matching methods, exhibit higher PEI values than CLP-CFF, suggesting that there is still room for efficiency improvement in phase-based methods.

3.2. The measurement of seismic response of the cold-formed steel wall (CSW) structure

To further evaluate the effectiveness of the proposed CLP-CFF approach, we employed experimental data from a large-scale outdoor shake table test on a cold-formed steel wall (CSW) system subjected to simulated seismic loading, made available through an open-access repository. The experiment took place at the Large High Performance Outdoor Shake Table (LHPOST) located at the University of California, San Diego (UCSD), USA, as described in (Singh et al., 2023).

The test specimens were configured based on prototype designs representative of four- and ten-story buildings, ensuring alignment with previously published experimental studies. Each test wall was arranged in a shear–gravity–gravity–shear sequence, and tie rods were installed at both ends of each shear wall segment. Steel sheet sheathing was attached according to a defined fastening layout to replicate field construction standards. Detailed setup information, test documentation, and datasets can be accessed through the DesignSafe data repository (Singh et al., 2023).

An overview of the experimental layout is shown in Fig. 9. The LHPOST delivered seismic input using the CNP196 component from the Canoga Park recording of the 1994 Northridge earthquake (magnitude Mw = 6.7). A digital video recorder (DVR) was mounted perpendicular to the shake table's motion direction to monitor the global structural behavior. The camera captured high-definition footage at 1920 × 1080 resolution and 30 frames per second. A pixel-to-length conversion ratio of 4.4418 mm/pixel, obtained through calculating the ratio between a known physical length of the structure and its corresponding pixel length in the reference frame, was used in this study (Cai et al., 2024).

To support the application of a vision-based displacement tracking technique, a visual marker was mounted on the upper part of the CSW structure. Additionally, string potentiometers were mounted laterally on the transfer beam near the top to measure horizontal displacements, serving as reference data. These analog sensors sampled data at 256 Hz, providing ground truth for evaluating the vision-based measurement approach.

To enable a direct comparison on displacement signals between camera and string potentiometer, the two signals were first synchronized in the time domain by aligning their corresponding initial response features. Subsequently, the string potentiometer signal was resampled to match the sampling frequency of the camera system.

The same range of standard deviation values as in the previous section is also employed to study the performance of the CLP-CFF method in this real-life structural experiment. The displacement measurement results for all standard deviation values are presented in Table 7.

In this case, the MAE also exhibits a trend of first decreasing and then increasing as the standard deviation increases. Similarly, within the range of 2.0 to 2.8, the overall measurement accuracy remains relatively high and exceeds that of most other methods in Table 8. The main difference from the experiment in the previous section is that the extremum point appears around 2.15. The decrease from the previous value of 2.35 can be attributed to the presence of small-amplitude vibrations in addition to large-scale motion in this measurement scenario. As a result, it is necessary to sacrifice a small amount of Hilbert transform precision to enhance edge localization capability, allowing more accurate detection of these minor vibrations and thus improving the overall accuracy. The extremum point in this case is also selected for subsequent plotting and comparison.

It should be noted that, in this study, the optimal standard deviation is identified by comparison with ground truth data, with the aim of demonstrating the upper-bound performance of the proposed CLP-CFF method. In practical applications where ground truth is unavailable, an automatic or adaptive strategy for determining the optimal standard deviation requires further investigation. Nevertheless, in practical

Table 6
The comprehensive performance of different vision-based methods for the laboratory experiment.

	CSP	Gabor	Hilbert	Riesz	Derivative	LK	TM	RFAT	CLP-CFF
PEI (dimensionless, $\alpha = 6$, $\beta = 1$)	15.7117	27.7136	2.3362	0.0395	0.0000	6.6696	3.7089	1.8539	118.5227
PEI (dimensionless, $\alpha = 4$, $\beta = 1$)	1.0386	1.4268	0.3087	0.0207	0.0000	1.4279	0.9719	0.2589	7.0911
PEI (dimensionless, $\alpha = 2$, $\beta = 1$)	0.0686	0.0735	0.0408	0.0108	0.0002	0.3057	0.2547	0.0361	0.4243
PEI (dimensionless, $\alpha = 1$, $\beta = 1$)	0.0176	0.0167	0.0148	0.0078	0.0016	0.1414	0.1304	0.0135	0.1038

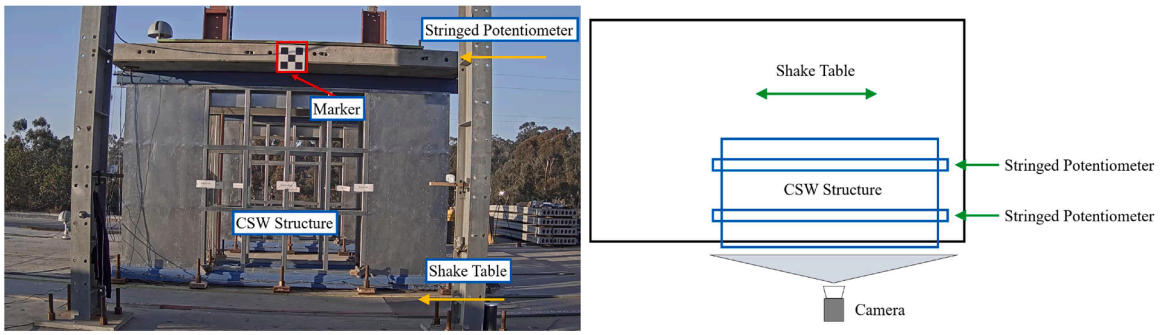

(a) Experiment layout (b) Schematic diagram

Fig. 9. Experimental layout of the shaking table test of the CSW structure (adapted from (Singh et al., 2023)).

Table 7
The measurement performance of the CLP-CFF method with various standard deviations for the shaking table test of the CSW structure.

Standard Deviation	1.00	1.20	1.50	1.80	2.00	2.10	2.15	2.20	2.30
MAE (mm)	7.2230	5.3763	3.0827	1.7501	1.3788	1.3156	1.2996	1.3066	1.3258
Standard Deviation	2.40	2.50	2.60	2.70	2.80	2.90	3.00	3.20	3.50
MAE (mm)	1.3636	1.4116	1.4672	1.5296	1.5990	1.6722	1.7487	1.9072	2.1328

Table 8
MAE comparison between different vision-based methods for the shaking table test of the CSW structure.

	CLP-CFF	Gabor	CSP	Hilbert	Riesz	Derivative	LK	TM	RAFT
MAE(mm)	1.2996	1.1404	1.3397	6.4154	4.8023	15.5743	2.6180	2.8131	5.8719

scenarios, the standard deviation can be selected within a practical range (2.0-2.8). Although such a choice may not achieve the optimal performance of the CLP-CFF method, it generally yields high measurement accuracy and can still outperform most existing methods.

The displacement measurement results obtained using the CLP-CFF method are presented in Fig. 10. The estimated displacements closely match the ground truth data recorded by the string potentiometer, demonstrating the high fidelity and accuracy of the proposed approach.

Various vision-based methods, including LK optical flow, template matching, RAFT optical flow, and both traditional and recently developed phase-based optical flow methods, are employed for comparison with the CLP-CFF method. The hyperparameters and implementation details are similar to the previous section. The results are presented in Table 8, with the MAE used as the accuracy metric. The displacement time histories for all methods are shown in Fig. 11.

As observed in Table 8, the CLP-CFF method consistently achieves high measurement accuracy in this real-world scenario, demonstrating its robustness under complex environmental conditions. In this study, robustness is implicitly evaluated through the ability to maintain high displacement measurement accuracy in non-ideal experimental settings. The outdoor experimental results further demonstrate that the proposed method delivers reliable and accurate measurements under real-world conditions, thereby validating its robustness.

As a newly proposed phase extraction method, CLP-CFF shows a significant improvement in accuracy compared to the recently developed phase-based methods and even achieves a slightly lower MAE than the CSP method.

As observed from the Fig. 11, the derivation-enhanced method also

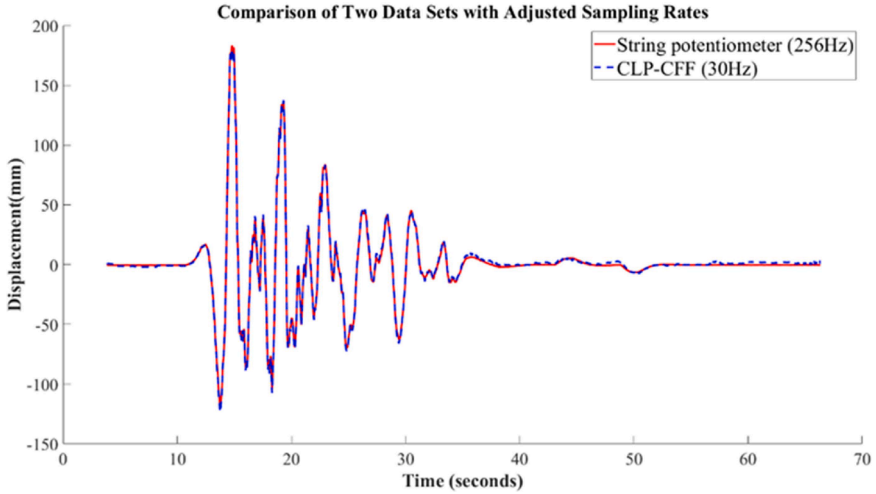

Fig. 10. The displacement measurement results from the CLP-CFF.

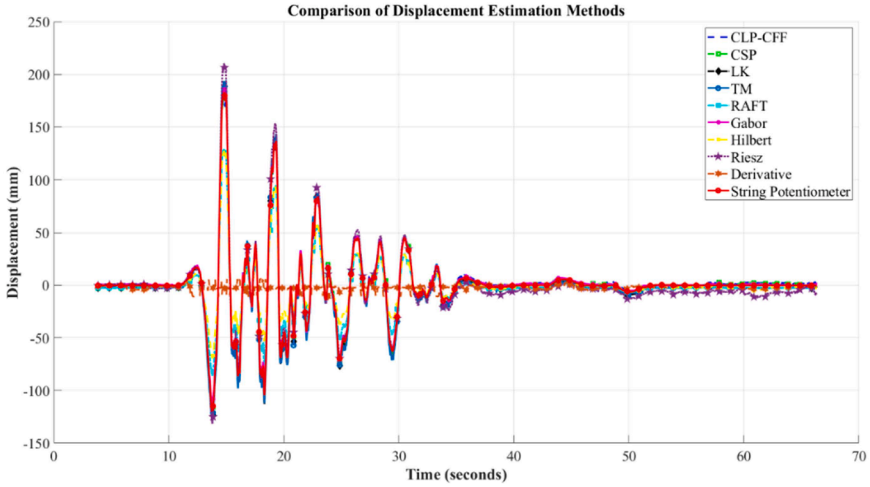

Fig. 11. Comparison of displacement history between vision-based methods and string potentiometer.

fails to perform adequately in this measurement task. Although the Hilbert-transform- and Riesz-transform-enhanced methods exhibit displacement trends that are generally consistent with the ground truth, their amplitude responses show significant deviations. This may be caused by the complexity of the video environment. In the video frames, the marker appears relatively small, and the CSW pattern is visually prominent. As a result, the frame may contain dominant frequency components unrelated to the target, which can be mistakenly identified as peak frequencies in their peak frequency selection strategies.

However, compared to its performance in the previous indoor experiment, the RAFT optical flow method exhibits significantly reduced accuracy, suggesting that it is less reliable in complex environments. It should be noted that the RAFT method was not fine-tuned using the experimental data in this study. This is primarily because the available ground truth displacement measurements are limited to a single point, whereas fine-tuning RAFT requires dense, full-field displacement data for supervision. In addition, the number of available structural motion videos is insufficient to form a representative dataset for meaningful training and testing. Fine-tuning under such conditions would essentially lead to ground-truth–guided optimization on the test cases rather than a training process reflecting the model's generalization capability.

These limitations highlight a general challenge of deep learning-based displacement measurement methods, which typically require large and diverse real-world datasets to achieve robust generalization. In contrast, the proposed CLP-CFF method is not data-driven but is derived from an interpretable theoretical framework for extracting displacement directly from video sequences, enabling stable measurement performance even under complex experimental conditions.

The computational efficiencies of different methods are compared under the same computational environment described in the previous section. The total number of frames in the processed video in this section is 1975. The processing time and speed are presented in Table 9. With accuracy comparable to that of traditional phase-based methods, the CLP-CFF method achieves significantly improved computational efficiency. Specifically, it is approximately 7 times faster than the Gabor wavelet method, 5 times faster than CSP, 4 times faster than the Hilbert and Riesz transform-enhanced methods, and 1.5 times faster than the derivative-enhanced method, making it the fastest phase-based method.

The PEI introduced in Section 3.1 is also employed in this full-scale outdoor experiment to evaluate the overall performance of the algorithm, with an emphasis on accuracy over efficiency. As shown in Table 10, CLP-CFF still achieves the highest PEI value among all phase-based methods across all cases, demonstrating its superior overall performance. However, when compared with intensity-based methods, CLP-CFF exhibits slightly lower PEI values than the LK optical flow and template matching methods when accuracy and efficiency are assigned equal weight, indicating that there remains room for improving the computational efficiency of phase-based methods in vision-based displacement monitoring.

Overall, the CLP-CFF method demonstrates a superior balance between accuracy and computational efficiency among all existing phase-based methods in this real-world application.

4. Conclusion

This paper presents a new phase extraction method, CLP-CFF, for phase-based displacement measurement. It retains the high accuracy of traditional phase-based methods while significantly improving computational efficiency. The CLP-CFF method is developed based on the Laplacian pyramid, which functions like a bandpass filter to aid in phase extraction. Furthermore, the focus frequency at each scale level of the Laplacian pyramid is adjusted to enhance the accuracy of phase extraction for displacement measurement. This enhanced version is referred to as the LP-CFF. Subsequently, the LP-CFF subbands are further processed using the Hilbert transform, resulting in the proposed CLP-CFF method. Finally, the performance of the CLP-CFF method, in terms of both accuracy and computational efficiency, is subsequently validated through laboratory and outdoor experiments by comparing it to other vision-based methods. Specifically, the CLP-CFF achieves accuracy comparable to traditional phase-based methods, while improving computational efficiency by a factor of at least 5. Moreover, the proposed CLP-CFF exhibits higher computational efficiency than other recently developed phase-based methods.

Owing to the significantly improved computational efficiency of the proposed CLP-CFF method over conventional phase-based approaches,

Table 9
The computation time comparison of different vision-based methods for the shaking table test of the CSW structure.

	CLP-CFF	Gabor	CSP	Hilbert	Riesz	Derivative	LK	TM	RAFT
Computation time(seconds)	92.2392	650.1925	483.1213	324.8478	393.7907	138.4298	38.0770	36.3007	449.1618
Processing speed(ms/frame)	49.1942	346.7693	257.6647	173.2522	210.0217	73.8292	20.3077	19.3604	239.5530

Table 10
The comprehensive performance of different vision-based methods for the shaking table test of the CSW structure.

	CLP-CFF	Gabor	CSP	Hilbert	Riesz	Derivative	LK	TM	RAFT
PEI (dimensionless, $\alpha = 6$, $\beta = 1$) $\times 10^{-4}$	22.5023	6.9922	3.5801	0.0004	0.0021	0.0000	0.8157	0.5559	0.0005
PEI (dimensionless, $\alpha = 4$, $\beta = 1$) $\times 10^{-4}$	38.0054	9.0935	6.4256	0.0182	0.0477	0.0012	5.5906	4.3989	0.0187
PEI (dimensionless, $\alpha = 2$, $\beta = 1$) $\times 10^{-4}$	64.1897	11.8262	11.5326	0.7480	1.1011	0.2978	38.3176	34.8109	0.6457
PEI (dimensionless, $\alpha = 1$, $\beta = 1$) $\times 10^{-4}$	83.4209	13.4865	15.4503	4.7984	5.2879	4.6383	100.3154	97.9264	3.7916

future work will focus on extending the method to real-time displacement monitoring systems. Benefiting from the inherent robustness of phase-based methods to illumination variations, the proposed approach has the potential to support both real-time and long-term structural displacement monitoring under practical field conditions. Such capabilities are expected to facilitate continuous structural health monitoring and contribute to the assessment and improvement of structural serviceability.

Funding information

China Scholarship Council, Grant/Award Number: 202106370030.

Declaration of competing interest

The authors declare the following financial interests/personal relationships which may be considered as potential competing interests:

Sida Ai reports financial support was provided by China Scholarship Council. If there are other authors, they declare that they have no known competing financial interests or personal relationships that could have appeared to influence the work reported in this paper.

Acknowledgment

This research was financially supported by the China Scholarship Council (No. 202106370030).

References

Ai, S., Dong, C., & Mei, Q. (2025). The optimal scale level of complex steerable pyramid for phase-based motion estimation under different motion ranges and target sizes. *Measurement, 253*, Article 117440. https://doi.org/10.1016/j.measurement.2025.117440

Amezquita-Sanchez, J. P., & Adeli, H. (2019). Nonlinear measurements for feature extraction in structural health monitoring. *Scientia Iranica. Transaction A, Civil Engineering, 26*(6), 3051–3059.

Barron, J. L., Fleet, D. J., & Beauchemin, S. S. (1994). Performance of optical flow techniques. *International Journal of Computer Vision, 12*(1), 43–77.

Burt, P. J., & Adelson, E. H. (1987). The Laplacian pyramid as a compact image code. *Readings in computer vision* (pp. 671–679). Elsevier. https://doi.org/10.1016/B978-0-08-051581-6.50065-9

Cai, E., Zhang, Y., Lu, X., Ji, X., Gao, X., Hou, J., Shi, J., & Guo, W. (2024). Estimating structural motions in extreme environmental conditions——A dynamic correlation filter based computer vision approach. *Mechanical Systems and Signal Processing, 215*, Article 111398. https://doi.org/10.1016/j.ymssp.2024.111398

Cai, E., Zhang, Y., & Quek, S. T. (2023). Visualizing and quantifying small and nonstationary structural motions in video measurement. *Computer-Aided Civil and Infrastructure Engineering, 38*(2), 135–159. https://doi.org/10.1111/mice.12894

Chen, J. G., Wadhwa, N., Cha, Y.-J., Durand, F., Freeman, W. T., & Buyukozturk, O. (2014). Structural modal identification through high speed camera video: Motion magnificationJ. De Clerck (Ed.), Structural modal identification through high speed camera video: Motion magnification. *Topics in modal analysis I, 7*, 191–197. https://doi.org/10.1007/978-3-319-04753-9_19

Chen, J. G., Wadhwa, N., Cha, Y.-J., Durand, F., Freeman, W. T., & Buyukozturk, O. (2015). Modal identification of simple structures with high-speed video using motion magnification. *Journal of Sound and Vibration, 345*, 58–71. https://doi.org/10.1016/j.jsv.2015.01.024

Chen, Y., Joffre, D., & Avitabile, P. (2018). Underwater dynamic response at limited points expanded to full-field strain response. *Journal of Vibration and Acoustics, 140*(5), Article 051016. https://doi.org/10.1115/1.4039800

Cohen, L. (1995). *Time frequency analysis*. Prentice Hall.

Collier, S., & Dare, T. (2022). Accuracy of phase-based optical flow for vibration extraction. *Journal of Sound and Vibration, 535*, Article 117112. https://doi.org/10.1016/j.jsv.2022.117112

Diamond, D. H., Heyns, P. S., & Oberholster, A. J. (2017). Accuracy evaluation of sub-pixel structural vibration measurements through optical flow analysis of a video sequence. *Measurement, 95*, 166–172. https://doi.org/10.1016/j.measurement.2016.10.021

Dong, C.-Z., & Catbas, F. N. (2021). A review of computer vision–based structural health monitoring at local and global levels. *Structural Health Monitoring, 20*(2), 692–743. https://doi.org/10.1177/1475921720935585

Feng, D., & Feng, M. Q. (2016). Vision-based multipoint displacement measurement for structural health monitoring: Vision-based displacement measurement for SHM. *Structural Control and Health Monitoring, 23*(5), 876–890. https://doi.org/10.1002/stc.1819

Feng, D., & Feng, M. Q. (2018). Computer vision for SHM of civil infrastructure: From dynamic response measurement to damage detection – A review. *Engineering Structures, 156*, 105–117. https://doi.org/10.1016/j.engstruct.2017.11.018

Fleet, D. J., & Jepson, A. D. (1990). Computation of component image velocity from local phase information. *International Journal of Computer Vision, 5*(1), 77–104. https://doi.org/10.1007/BF00056772

Gomez, F., Park, J.-W., & Spencer, B. F. (2018). Reference-free structural dynamic displacement estimation method. *Structural Control and Health Monitoring, 25*(8), e2209. https://doi.org/10.1002/stc.2209

Horn, B. K. P., & Schunck, B. G. (1981). Determining optical flow. *Artificial Intelligence, 17*(1–3), 185–203. https://doi.org/10.1016/0004-3702(81)90024-2

Javadinasab Hormozabad, S., Gutierrez Soto, M., & Adeli, H. (2021). Integrating structural control, health monitoring, and energy harvesting for smart cities. *Expert Systems, 38*(8), Article e12845. https://doi.org/10.1111/exsy.12845

Li, M. Z., Liu, G., Mao, Z., Yang, Q. S., & Gu, J. W. (2023). Two-dimensional motion estimation using phase-based image processing with Riesz transform. *Mechanical Systems and Signal Processing, 188*, Article 110044. https://doi.org/10.1016/j.ymssp.2022.110044

Liu, G., Li, M. Z., Mao, Z., & Yang, Q. S. (2022). Structural motion estimation via Hilbert transform enhanced phase-based video processing. *Mechanical Systems and Signal Processing, 166*, Article 108418. https://doi.org/10.1016/j.ymssp.2021.108418

Liu, S., Yu, L., Niu, W., Wang, J., Zhong, Z., Huang, J., & Shan, M. (2024). Fast and accurate visual vibration measurement via derivative-enhanced phase-based optical flow. *Mechanical Systems and Signal Processing, 209*, Article 111089. https://doi.org/10.1016/j.ymssp.2023.111089

Luan, L., Zheng, J., Wang, M. L., Yang, Y., Rizzo, P., & Sun, H. (2021). Extracting full-field subpixel structural displacements from videos via deep learning. *Journal of Sound and Vibration, 505*, Article 116142. https://doi.org/10.1016/j.jsv.2021.116142

Lucas, B. D., & Kanade, T. (1981). An iterative image registration technique with an application to stereo vision. In *, 2. Proceedings of the IJCAI'81: 7th international joint conference on artificial intelligence* (pp. 674–679). https://hal.science/hal-03697340.

Luo, L., & Feng, M. Q. (2018). Edge-enhanced matching for gradient-based computer vision displacement measurement. *Computer-Aided Civil and Infrastructure Engineering, 33*(12), 1019–1040. https://doi.org/10.1111/mice.12415

Ma, Z., Choi, J., Liu, P., & Sohn, H. (2022). Structural displacement estimation by fusing vision camera and accelerometer using hybrid computer vision algorithm and adaptive multi-rate Kalman filter. *Automation in Construction, 140*, Article 104338. https://doi.org/10.1016/j.autcon.2022.104338

Miao, Y., Jeon, J. Y., Kong, Y., & Park, G. (2022). Phase-based displacement measurement on a straight edge using an optimal complex Gabor filter. *Mechanical Systems and Signal Processing, 164*, Article 108224. https://doi.org/10.1016/j.ymssp.2021.108224

Miao, Y., Kong, Y., Nam, H., Lee, S., & Park, G. (2023). Phase-based vibration imaging for structural dynamics applications: Marker-free full-field displacement measurements with confidence measures. *Mechanical Systems and Signal Processing, 198*, Article 110418. https://doi.org/10.1016/j.ymssp.2023.110418

Morrone, M. C., & Owens, R. A. (1987). Feature detection from local energy. *Pattern Recognition Letters, 6*(5), 303–313. https://doi.org/10.1016/0167-8655(87)90013-4

Morrone, M. C., Ross, J., Burr, D. C., & Owens, R. (1986). Mach bands are phase dependent. *Nature, 324*(6094), 250–253. https://doi.org/10.1038/324250a0

Movellan, J. R. (2002). Tutorial on Gabor filters. *Open Source Document, 40*, 1–23.

Oh, B. K., Kim, K. J., Kim, Y., Park, H. S., & Adeli, H. (2017). Evolutionary learning based sustainable strain sensing model for structural health monitoring of high-rise buildings. *Applied Soft Computing, 58*, 576–585. https://doi.org/10.1016/j.asoc.2017.05.029

Pan, X., Yang, T. Y., Xiao, Y., Yao, H., & Adeli, H. (2023). Vision-based real-time structural vibration measurement through deep-learning-based detection and tracking methods. *Engineering Structures, 281*, Article 115676. https://doi.org/10.1016/j.engstruct.2023.115676

Park, S. W., Park, H. S., Kim, J. H., & Adeli, H. (2015). 3D displacement measurement model for health monitoring of structures using a motion capture system. *Measurement, 59*, 352–362. https://doi.org/10.1016/j.measurement.2014.09.063

Perez-Ramirez, C. A., Amezquita-Sanchez, J. P., Valtierra-Rodriguez, M., Adeli, H., Dominguez-Gonzalez, A., & Romero-Troncoso, R. J. (2019). Recurrent neural network model with Bayesian training and mutual information for response

prediction of large buildings. *Engineering Structures, 178*, 603–615. https://doi.org/10.1016/j.engstruct.2018.10.065

Saxena, S. C., & Seksena, S. B. L. (1989). A self-compensated smart LVDT transducer. *IEEE Transactions on Instrumentation and Measurement, 38*(3), 748–753. https://doi.org/10.1109/19.32186

Shang, Z., & Shen, Z. (2018). Multi-point vibration measurement and mode magnification of civil structures using video-based motion processing. *Automation in Construction, 93*, 231–240. https://doi.org/10.1016/j.autcon.2018.05.025

Simoncelli, E. P., & Freeman, W. T. (1995). The steerable pyramid: A flexible architecture for multi-scale derivative computation. In *, 3. Proceedings of the international conference on image processing* (pp. 444–447). https://doi.org/10.1109/ICIP.1995.537667

Simoncelli, E. P., Freeman, W. T., Adelson, E. H., & Heeger, D. J. (1992). Shiftable multiscale transforms. *IEEE Transactions on Information Theory, 38*(2), 587–607. https://doi.org/10.1109/18.119725

Singh, A., Hutchinson, T., Wang, X., Zhang, Z., Schafer, B., Derveni, F., Castaneda, H., & Peterman, K. (2023). *Wall line tests: Phase 1 – Shake table tests: in CFS-NHERI: seismic resiliency of repetitively framed mid-rise cold-formed steel buildings (Version 2)*. Designsafe-CI. https://doi.org/10.17603/DS2-MVJ8-8386. </Dataset>.

Teed, Z., & Deng, J. (2020). RAFT: Recurrent all-Pairs field transforms for optical flow. In A. Vedaldi, H. Bischof, T. Brox, & & J.-M. Frahm (Eds.), *Computer vision – ECCV 2020: 12347. Computer vision – ECCV 2020* (pp. 402–419). Springer International Publishing. https://doi.org/10.1007/978-3-030-58536-5_24.

Xu, Y., & Brownjohn, J. M. W (2018). Review of machine-vision based methodologies for displacement measurement in civil structures. *Journal of Civil Structural Health Monitoring, 8*(1), 91–110. https://doi.org/10.1007/s13349-017-0261-4

Yang, J., & Tse, P. (2021). Sparse representation of complex steerable pyramid for machine fault diagnosis by using non-contact video motion to replace conventional accelerometers. *Measurement, 175*, Article 109104. https://doi.org/10.1016/j.measurement.2021.109104